Journal of CO2 Utilization 70 (2023) 102431

Contents lists available at ScienceDirect

Journal of CO2 Utilization

journal homepage: www.elsevier.com/locate/jcou

Continuous carbon dioxide electroreduction to formate coupled with the single-pass glycerol oxidation to high value-added products

Kevin Fernández-Caso [a], Ailen Peña-Rodríguez [b], José Solla-Gullón [b], Vicente Montiel [b], Guillermo Díaz-Sainz [a,*], Manuel Alvarez-Guerra [a], Angel Irabien [a]

[a] Departamento de Ingenierías Química y Biomolecular, Universidad de Cantabria, Avda. Los Castros, s/n, 39005 Santander, Spain
[b] Instituto de Electroquímica, Universidad de Alicante, Apdo. 99, E-03080 Alicante, Spain

ARTICLE INFO

Keywords:
Continuous CO_2 electroreduction
Formate
Single pass glycerol oxidation reaction
Dihydroxyacetone

ABSTRACT

CO_2 electroreduction has been considered a promising alternative to simultaneously reduce CO_2 emissions and produce value-added products. Among others, the production of formic acid/formate is particularly attractive. Although promising results have already been obtained in the literature, one of the recent approaches to improve the process deals with the use of an alternative reaction at the anode instead of the traditional oxygen evolution reaction (OER). In this context, this work reports, for the first time, the study of the CO_2 electroreduction to formate coupled with the electrooxidation of glycerol to high-added value products where both half-reactions operate in a continuous mode with a single pass of the reactants through the electrochemical cell. Interestingly, at the cathode, similar results to those previously reported were obtained, reaching formate concentrations of about 18 $g{\cdot}L^{-1}$ at a 200 $mA{\cdot}cm^{-2}$. In addition, at the anode, promising dihydroxyacetone productions of 196 $\mu mol{\cdot}m^{-2}{\cdot}s^{-1}$ were simultaneously achieved in the output stream of the anodic compartment. These findings represent a significant step forward for the development and application of the technology.

1. Introduction

CO_2 electrocatalytic reduction powered by renewable sources (e.g. solar or wind) represents a hopeful alternative to decrease greenhouse emissions to the atmosphere and obtain value-added products [1,2]. In this sense, CO_2 electrolysis to chemicals like formic acid (HCOOH) or formate ($HCOO^-$), is gaining attention since these products have a large number of uses in some conventional industries and they can also be employed as hydrogen carrier molecules or reagents for direct HCOOH or $HCOO^-$ low-temperature fuel cells [3–5]. Despite great efforts focused on the implementation of batch [6,7] or semi-batch [8,9] CO_2 electrolysers, continuous operation is desirable for the further development of these processes at an industrial scale [10]. Promising results have already been achieved by some relevant studies in the last years [11–16], but some challenges have still to be overcome for the practical application of this technology [17], ensuring a positive performance both from environmental and economic points of view [18,19]. In this way, the electrochemical production of HCOOH or $HCOO^-$ from CO_2 should combine excellent Faradaic Efficiencies (FE) towards the target product, high production rates, and low overpotentials to ensure a commercially viable process, as well as to obtain product concentrations close to 85% wt. by using electrocatalysts with higher stabilities [20].

Most of the recent efforts made in the electrochemical conversion of CO_2 to $HCOO^-$ have been focused on the improvement of the performance of cathode, mainly through the use of new nanoparticulate electrocatalysts and different physical configurations of electrodes. In this sense, most of these studies have carried out the oxygen evolution reaction (OER) simultaneously at the anode [21–24]. Nevertheless, the main disadvantage of pairing the OER with the CO_2 electroreduction is the low oxygen market price and the high cell potential associated [25]. A way of improvement is to study the coupling of an anodic reaction of interest to the CO_2 electrochemical reduction reaction, as some references have recently published [25–27]. Some of the anodic reactions of interest and their main characteristics are summarised in Table S1 in the Supporting Information. First, Sabatino et al.[28] carried out the continuous CO_2 electrochemical reduction to $HCOO^-$ with the simultaneous oxidation of acid orange 7 solution (azoic dye resistant to conventional biological processes) employing a Boron Doped Diamond as a counter electrode. In addition, Wang et al.[29] employed an Co_3O_4-coated graphite anode for the oxidation of methyl orange reaching

* Corresponding author.
E-mail address: diazsg@unican.es (G. Díaz-Sainz).

https://doi.org/10.1016/j.jcou.2023.102431
Received 8 December 2022; Received in revised form 3 February 2023; Accepted 13 February 2023
Available online 15 February 2023

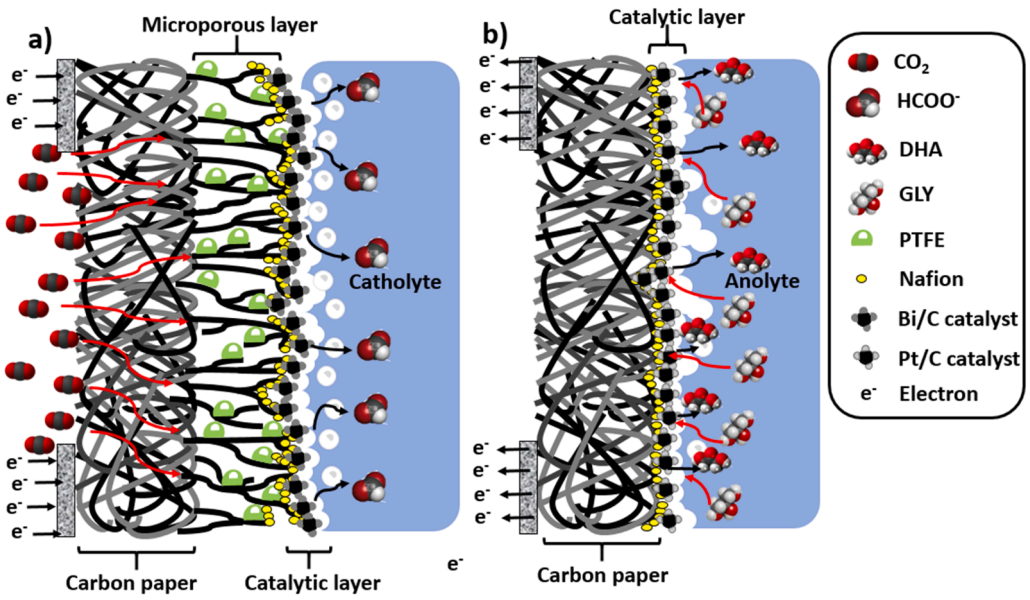

Fig. 1. Schematic representation of a a) Bi/C-GDE as working electrode and b) Pt/C-PE as counter electrode.

promising removal Efficiencies of the chemical oxygen demand in the anode compartment of up to 30%. In contrast, Bevilacqua et al. [30] coupled the ethanol oxidation reaction to CO_2 electrolysis, reducing the absolute cell potentials and therefore energy consumptions (from 130 to 77 kWh per kg of hydrocarbon product mixture), in comparison to the potential operating with oxygen evolution reaction. Besides, Wu et al. [31] implemented a continuous electrochemical reactor in which $HCOO^-$ was co-produced in both compartments from CO_2 (cathode) and methanol (anode), achieving promising results in terms of energy consumption of 90 kWh per kmol of $HCOO^-$. In a similar way, Zhang et al.[32] co-produced efficiently $HCOO^-$ from both CO_2 reduction and methanol oxidation reactions during long periods of time (>30 h) at absolute cell potentials of 2.6 V. Li and co-workers [33] obtained ultralow absolute cell potentials of 0.86 V at current densities of 100 $mA{\cdot}cm^{-2}$ by pairing the formaldehyde oxidation reaction to continuous CO_2 reduction for the co-production of $HCOO^-$ in a flow-cell.

Interestingly, recent techno-economic approaches claim that glycerol oxidation reaction (GOR) coupled to the CO_2 electroreduction ($ERCO_2$) process can involve excellent environmental and economic potential benefits [26,27]. Glycerol is a plentiful by-product of the transesterification process of biodiesel production, and therefore it is desirable to valorise this surplus [34]. First, Verma et al.[26] studied the GOR coupled to CO_2 electrochemical reduction reaction, showing some potential benefits like the reduction of electricity consumption by up to 53% with respect to the OER. Moreover, Rumayor et al. [27] demonstrated that co-production of $HCOO^-$ from CO_2 in the cathode and the dihydroxyacetone (DHA) from GOR in the anode can be economically feasible. According to this analysis, DHA concentrations higher than 1.5 wt% in the anode are required in short-mid-term developments to achieve a positive decarbonisation scenario for the integrated production of DHA and $HCOO^-$ with respect to the traditional route [27]. The downstream DHA purification step can imply an energy consumption penalty, involving 74% of the carbon footprint value for the coupled electrochemical system feasibility, being the main hot spot of this novel decarbonization approach [27]. In general, DHA is mainly produced by the traditional route based on the glycerol *Gluconobacter oxidans* biofermentation in a two-stage fed-batch reactor with low productivities of 2.9 $gDHA{\cdot}L^{-1}{\cdot}h^{-1}$ due to long fermentation times (about 77 h) [35–37]. In addition to DHA, the GOR also permits obtaining a wide range of value-added products in alkaline media including oxalate (OA), glycerate (GLCA), glyceraldehyde (GLAD), $HCOO^-$, mesoxalate (MOX), glycolate (GLYC), lactate (LAC), among others [38].

Although the GOR has been deeply studied coupled with the hydrogen evolution reaction (HER) (Table S2 in Supporting Information), few attempts of coupling the GOR with the CO_2 reduction reaction at the cathode have been reported (Table S2 in Supporting Information). In this sense, Wang et al.[39] and Houache et al.[40] obtained CO from CO_2 in the cathode and oxidizing glycerol to $HCOO^-$ in the anode employing a two-compartment flow-reactor configuration. Khan et al. [41] performed the CO_2 reduction reaction to a gaseous product such as ethylene (employing a Cu-based catalysts on a polytetrafluoroethylene (PTFE) substrate), at the same time, the GOR took place at the anode to produce different products such as $HCOO^-$, glycolate, among others. In contrast, Pei et al.[42] developed the $ERCO_2$ to $HCOO^-$ process, carrying out the glycerol oxidation in the anode in a discontinuous mode, achieving promising results in terms of energy efficiency conversion of electricity to $HCOO^-$ (110%). Another promising approach realised by Guo and co-workers [43] allowed to co-produce $HCOO^-$ in both cathode (from $ERCO_2$) and anode (from GOR) with an energy saving of 91 kWh per kmol of $HCOO^-$ (compared to 247 kWh per kmol of $HCOO^-$ obtained with the OER) in a flow reactor equipped with an anion exchange membrane. However, as shown in Table S2, this previous literature has not worked in the continuous CO_2 reduction reaction to $HCOO^-$ at the cathode coupled with the GOR to high value-added products of 3 carbons at the anode.

In this context, here we study for the first time the coupling of continuous GOR to high value-added products of 3 carbons with the $ERCO_2$ towards $HCOO^-$ working with a single-pass of the reactants through the flow-cell electrochemical reactor, using Bi and Pt nanoparticles as electrocatalysts at the cathode and anode, respectively. Glycerol conversion was estimated and up to seven glycerol oxidation products have been detected in the anolyte output stream with the aim of determining the carbon balance of such a complex reaction as GOR. In addition, the influence of some key variables like the anolyte flow per geometric surface area and the current density on the performance of the cathode of the process, and at the same time, the glycerol oxidation products distribution was also systematically evaluated to assess the performance of coupling the GOR with the $ERCO_2$.

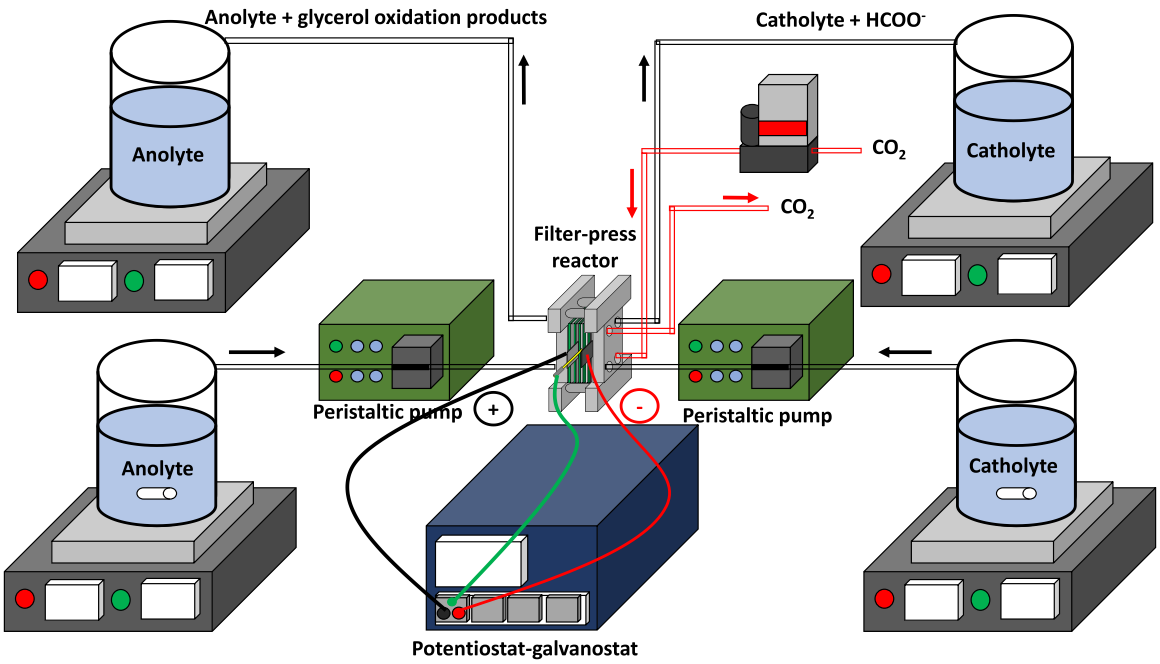

Fig. 2. Experimental set-up scheme employed for coupling the single pass GOR to the continuous $ERCO_2$ process to give formate.

2. Methodology

2.1. Electrodes fabrication and characterisation

Details on the synthesis and characterisation of the carbon-supported Bi nanoparticles (Bi/C NPs) used as cathode electrocatalysts as well as the subsequent manufacture and characterisation of the gas diffusion electrodes containing these Bi nanoparticles (Bi/C-GDE) can be found in previous contributions [14,44]. Very briefly, the Bi/C-GDE is composed of a carbonaceous support (Teflonated Toray carbon paper TGP-H-60), a microporous layer (MPL), and a catalytic layer (CL), as shown in Fig. 1a. The MPL was air-brushed over the Toray carbon paper support. The MPL ink was prepared with Vulcan XC-72R and PTFE (Polytetrafluoroethylene preparation, 60 wt% dispersion on H_2O, Sigma Aldrich) in a mass ratio of 40/60, and then diluted in isopropanol in a final slurry of 3 wt%. The ink was sonicated for 30 min before it was sprayed with the air-brusher. When the MPL reached a Vulcan XC-72R loading of 2 $mg{\cdot}cm^{-2}$, both layers were sintered at 350 ° C for 30 min. Subsequently, the CL was sprayed over the MPL by using the same technique. The catalytic ink consisted of Bi/C NPs in Nafion (Nafion D-521 dispersion, 5 w/w % in water and 1-propanol, 0.92 $meq{\cdot}g^{-1}$ exchange capacity) with a mass ratio of 70/30, which were then diluted in isopropanol and sonicated in the same conditions as described previously for the MPL. The Bi/C NPs loading was 0.75 $mg{\cdot}cm^{-2}$, as in previous studies for sake of comparison.

Commercial carbon-supported Pt nanoparticles (Pt/C) (20 wt%, particle size ≤5 nm, Sigma Aldrich) were employed as anode electrocatalysts. In this case, the carbon-supported Pt nanoparticles were directly deposited, using a similar methodology than that used for the catalytic later of the Bi/C-GDEs, onto a carbonaceous support (TGP-H-60) to form a Pt particulate electrode (Pt/C-PE) (Fig. 1b). The Pt loading deposited over the carbonaceous support was 1.00 $mg{\cdot}cm^{-2}$.

The Pt/C-PE electrodes were characterised by scanning electron microscopy (SEM, microscope JEOL, IT500HR/LA with EDS detector) to evaluate how the catalytic inks cover the Toray paper substrates and the dispersion of the Pt nanoparticles. Also, these electrodes were electrochemically characterised by cyclic voltammetry (CV) in an electrochemical glass cell using a standard three-electrode configuration. The

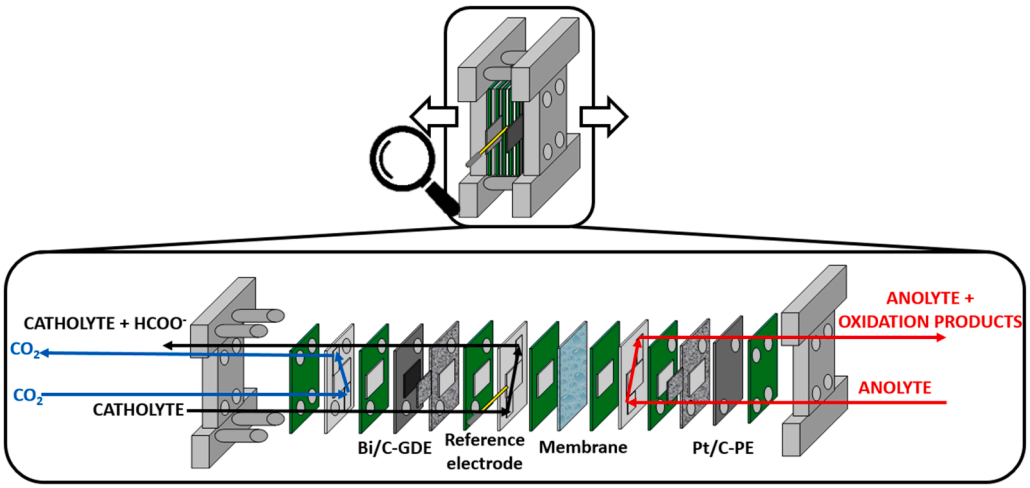

Fig. 3. Schematic illustration of CO_2 filter press reactor with stacked components.

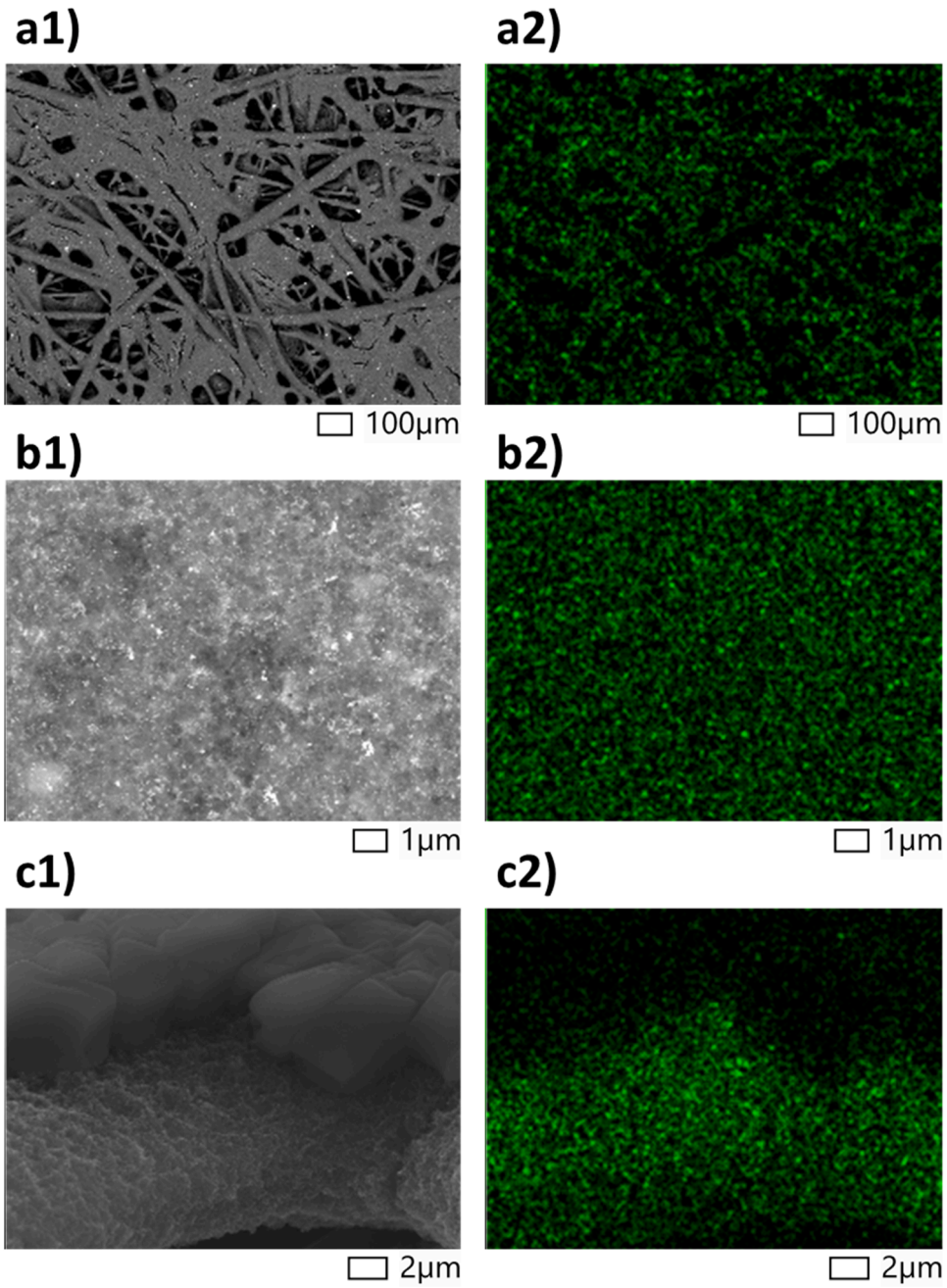

Fig. 4. Back-scattered electrons field emission SEM/EDS images (surface (a and b) and cross section (c)) of the Pt/C-PE electrodes with a 1 mg cm^{-2} metal loading.

electrolyte solution was an Ar saturated 0.5 M H_2SO_4 solution and a platinum wire and a reversible hydrogen electrode (RHE) were used as counter and reference electrodes, respectively. The experiments were carried out using a PGSTAT30 system (Metrohm Autolab B. V.) at ambient temperature.

2.2. Experimental setup

The Bi/C-GDE and Pt/C-PE prepared and characterised were then used as working (cathode) and counter (anode) electrodes, respectively, with a geometric surface area of 10 cm^2 each, in a continuous filter press electrochemical reactor. In addition to the filter press reactor as core element, the experimental set-up included peristaltic pumps (Watson Marlow 320, Watson Marlow Pumps Group), tanks and a potentiostat-galvanostat (Arbin Instruments, MSTAT4), as shown in Fig. 2.

Regarding the inputs of the electrochemical reactor, on the one hand, the electrolyte used in the cathodic compartment was a solution of 0.5 M KCl (potassium chloride, pharma grade, PanReac AppliChem) + 0.45 M $KHCO_3$ (potassium hydrogen carbonate, pharma grade, PanReac AppliChem). Moreover, pure CO_2 was fed to the cathodic compartment at a flow rate of 200 mL·min^{-1}, similar as previous studies in the group [44–47]. On the other hand, the anolyte was an aqueous solution of 1.0 M KOH (potassium hydroxide, 85% purity, pharma grade, PanReac AppliChem) + 1.0 M GLY (glycerol, 99% purity, ReagentPlus, Sigma Aldrich).

Fig. 3 illustrates the scheme of the internal structure of the filter press reactor configuration with stacked components (Micro Flow Cell, ElectroCell, A/s). Both cathodic and anodic compartments of the CO_2 electrolyser are separated by a Nafion 117 cationic exchange membrane (Alfa Aesar). As reference electrode, a leak-free Ag/AgCl 3.4 M KCl was placed close to the working electrode, in the cathodic compartment.

All the experiments were performed at least by duplicate with a

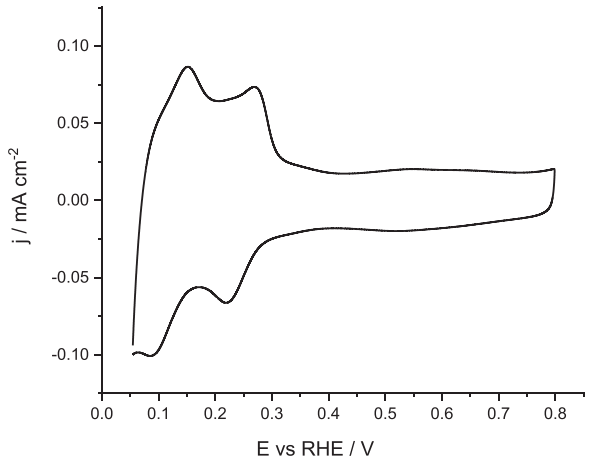

Fig. 5. Cyclic voltammetry response of the Pt/C-PE electrode with a loading of 1 mg cm^{-2} in Ar saturated 0.5 M H_2SO_4 solution. Scan rate 50 mV s^{-1}.

duration of time of 60 min in a continuous mode with a single pass of reactants through the electrochemical reactor, both in the cathodic and the anodic compartments. Moreover, all the tests were carried out at ambient conditions of pressure and temperature. Every 15 min, different samples of catholyte and anolyte were taken, in which the $HCOO^-$ and glycerol concentrations, respectively, were measured. Samples of the anolyte were neutralised with a solution of 1.0 M H_2SO_4 (Sulfuric acid, 98% purity, pharma grade, PanReac AppliChem) to facilitate the subsequent measurement of DHA and GLAD concentrations in alkaline media.

2.3. Analytical techniques

$HCOO^-$ concentration in the catholyte and anolyte was analysed by ion chromatography (Dionex ICS equipped with AS9 – HC column, using Na_2CO_3 as the eluent with a concentration, flow rate, conductivity and pressure of 4.5 mM, 1 mL·min^{-1}, 15 μS and 1800 psi, respectively). Glycerol oxidation products (such as DHA, GLAD, LAC, MOX and GLYC) have been detected and quantified by High Performance Liquid Chromatography (HPLC Agilent 1100 series VWD) equipped with a diode detector (Agilent 1260 Infinity II, 210 nm) and ion exchange column composed of a sulfonated styrene/divinylbenzene monodisperse matrix (Hi-Plex-H, 300 ×7.7 mm, Agilent). The eluent consisted of an aqueous phase solution of 5 mM H_2SO_4 and an organic phase of Acetonitrile (Acetonitrile CHROMASOLV™ Plus, for HPLC ≥99.9%) in a volumetric ratio of 94/6 v/v %, respectively. A constant eluent flow rate of 0.6 mL·min^{-1} was fixed and the column temperature was set at 50 ºC. The injection volume was established at 50 μL for all samples. Glycerol concentration in the output stream was measured by Attenuated Total Reflection (ATR, PerkinElmer) - Fourier-Transform Infrared Spectroscopy (FTIR, PerkinElmer) at wavelength ranges between 1000 and 1100 cm^{-1}. Finally, a total organic carbon analyser (TOC) was used to quantitatively measure the concentration of carbonates (CARB) in form of inorganic carbons presented in the output stream of the anodic compartment.

The average concentration value of all compounds has been calculated and the figures of merit employed for assessing the performance of the overall electrochemical process (Tables 3–11 of SI) and their equations have been reported in the Eqs. 1–5 of SI.

3. Results and discussion

3.1. Electrodes characterisation

As stated in the experimental section, a detailed characterisation of the Bi/C NPs used as cathode electrocatalysts and the gas diffusion electrodes containing these Bi nanoparticles (Bi/C-GDE) has already been reported in previous contributions [14,44,48]. Fig. 4 shows some representative (surface (Fig. 4a and b) and cross (Fig. 4c) section) SEM/EDS images of the Pt/C-PE electrodes. The SEM images display an optimal and homogeneous distribution of the carbon supported Pt nanoparticles onto the carbon fibres of the Toray paper leading to the formation of a uniform and compact catalytic layer. In addition, EDS analyses confirm the good homogeneity and dispersion of the Pt nanoparticles. Additional SEM/EDS images are included in the Supporting Information. Cross section SEM images of the electrodes (Fig. S1) that the thickness of the catalytic layer is about 25 μm.

The electrochemical characterisation of the Pt/C-PE electrode is reported in Fig. 5. The voltammetric response of the electrode in 0.5 M H_2SO_4 shows the characteristic voltammetric profile associated with a polyoriented Pt surface [49,50]. In brief, the signals observed between 0.05 and 0.4 V are attributed to the so-called hydrogen adsorption-desorption. It is worth noting that these voltametric features display a certain irreversibility which is due to the thickness of the catalytic layer (≈ 25 μm) which induce some limitation on the accessibility of the reactants to the inner part of the electrode [51]. The region from 0.4 to 0.8 V corresponds to a double layer region and any characteristic feature is visible. The electroactive surface area of the Pt/C-PE electrode was determined by the charge involved in the so-called hydrogen region assuming 0.21 mC cm^{-2} for the total charge after the subtraction of the double layer charging contribution. For a portion of the electrode of about 0.9 cm^2 of geometric area, a value of about 80 cm^2 of electroactive surface area was calculated.

3.2. Assessment of the glycerol oxidation products distribution: influence of the anolyte flow rate per geometric surface area

This section will focus on analyzing the products found in the anodic compartment, as well as the influence of the anolyte flow on that distribution of glycerol oxidation products. The main products detected in the anolyte output stream with 3 carbons were the GLAD, the DHA, the LAC and the MOX, while the only product quantified with 2 carbons was the GLYC. Finally, the most oxidised products measured with only 1 carbon were $HCOO^-$ and CARB.

Firstly, working for the $ERCO_2$ to $HCOO^-$ with a current density and an anolyte flow rate per geometric anode surface area of 45 mA·cm^{-2} and 0.57 mL·min^{-1}·cm^{-2}, respectively, the GOR was simultaneously carried out on the anode with an excellent performance, reaching a glycerol conversion of 2.45% and a carbon balance of 1.15%. Moreover, the different products detected in the anolyte output stream included LAC, GLAD, MOX, GLYC, $HCOO^-$ and CARB. First, $HCOO^-$, LAC and GLAD reached notable concentrations of 398, 256 and 396 mg·L^{-1}, respectively, while MOX, GLYC and CARB were also identified with lower concentrations of 135, 159 and 44 mg·L^{-1}, respectively. Based on these measurements, interesting Faradaic Efficiencies towards $HCOO^-$ (33.2%), LAC (11.6%), GLAD (13.9%), MOX (18.5%), CARB (5.4%) and GLYC (11.2%) were obtained, thus reaching an accumulated Faradaic Efficiency in the anode close to 94%. The reduction in the overall Faradaic Efficiency could be associated to trace amounts of CO_2 from the GOR and/or oxygen (O_2) from the competitive OER [52]. These results are detailed in Tables S4-S10 as Supporting Information.

Besides, operating with a current density of 90 mA·cm^{-2} and an anolyte flow rate per geometric anode surface area of 0.15 mL·min^{-1}·cm^{-2}, the glycerol conversion increased up to 21.08%, much higher than that obtained under previous experimental conditions, although the carbon balance also increased to 19.1%. LAC, GLAD, MOX, GLYC, $HCOO^-$ and CARB were obtained in the anolyte outlet stream in these operation conditions. Specifically, $HCOO^-$ and GLAD concentrations of 553 and 579 mg·L^{-1} were achieved, respectively. In smaller quantities, LAC, GLYC, CARB and MOX were also identified, reaching values of concentrations of 256, 269, 249 and 72 mg·L^{-1}, respectively. Moreover,

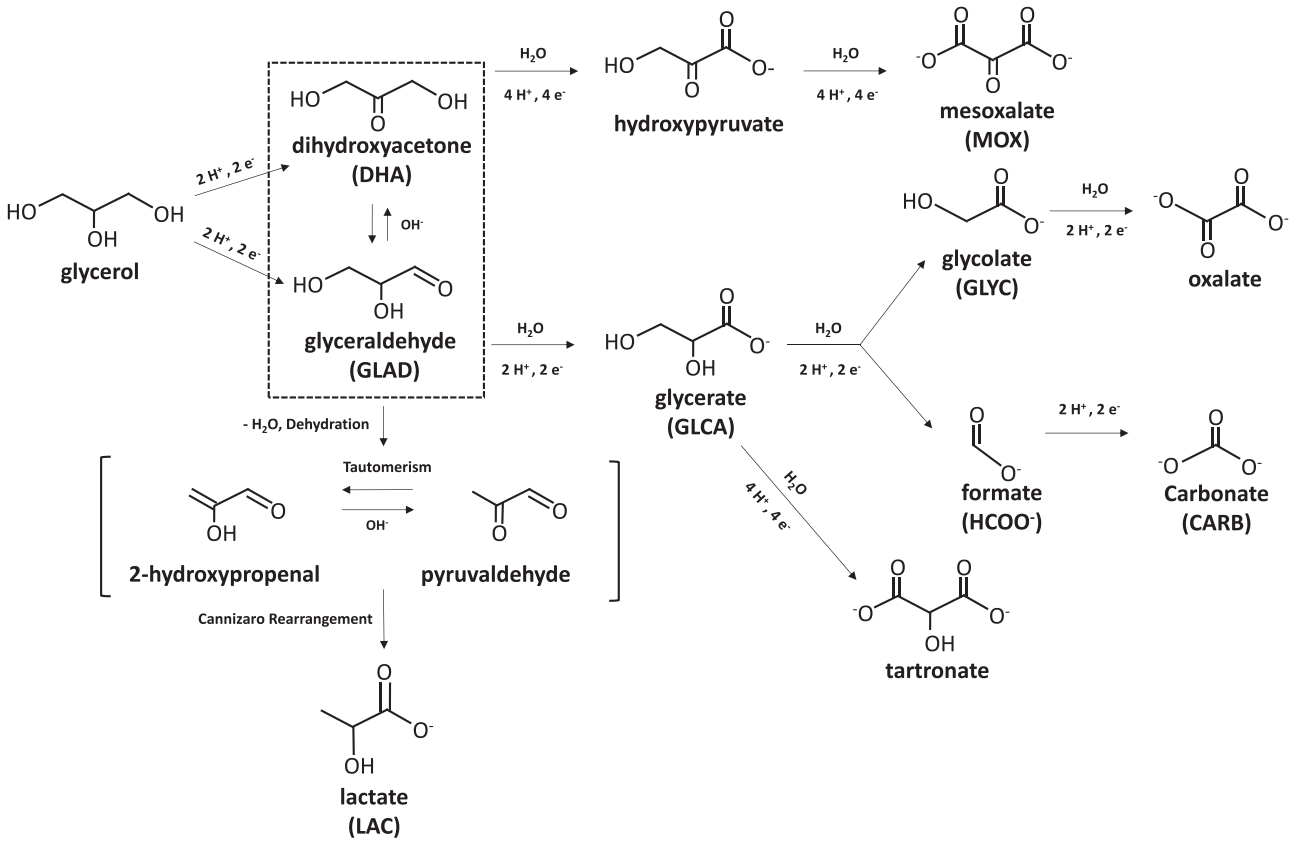

Fig. 6. Possible reaction pathways for the GOR in alkaline conditions. Adapted from ref. [56].

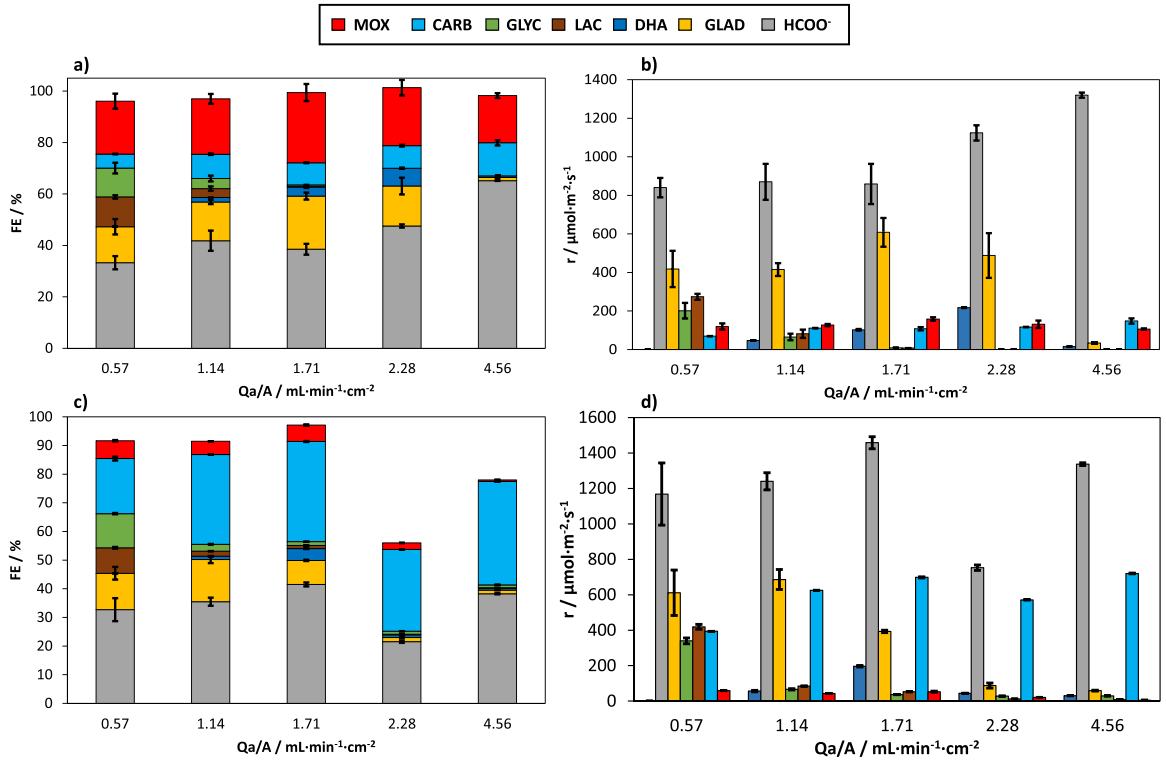

Fig. 7. a) Faradaic Efficiencies (FE) and b) production rates (r) of the glycerol oxidation products quantified as a function of the anolyte flow rate per geometric anode surface area (Qa/A) at current densities (j) of 45 mA·cm^{-2}; c) Faradaic Efficiencies (FE) and d) production rates (r) of the glycerol oxidation products quantified as a function of the anolyte flow rate per geometric anode surface area (Qa/A) at current densities (j) of 90 mA·cm^{-2}.

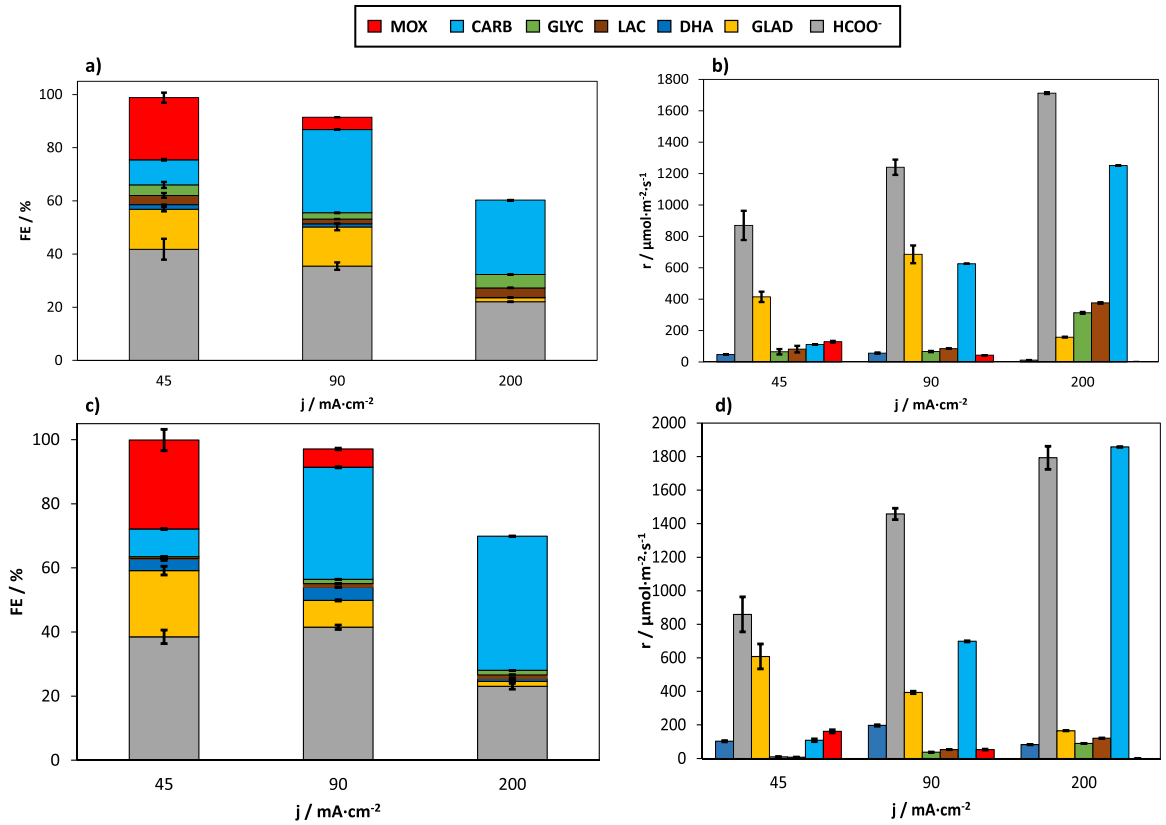

Fig. 8. a) Faradaic Efficiencies (FE) and b) production rates (r) of the glycerol oxidation products as a function of the current density (j) for different anolyte flow rates per geometric anode surface area (Qa/A) of 1.14 mL·min^{-1}·cm^{-2}; c) Faradaic Efficiencies (FE) and d) production rates (r) of the glycerol oxidation products as a function of the current density (j) for different anolyte flow rates per geometric anode surface area (Qa/A) of 1.71 mL·min^{-1}·cm^{-2}.

Faradaic Efficiencies of these oxidation products were similar as in the previous conditions considered, with the exception of the Faradaic Efficiencies of the CARB (19.2%) and the MOX (6.2%), reaching an accumulated Faradaic Efficiency close to 91.6%. In this way, C3 products such as MOX are re-oxidised to simpler products. Supplying current densities up to 90 mA·cm^{-2} generates higher potentials and therefore major amounts of the most oxidised compounds (e.g. CARB). The detailed results of this section, as well as the potentials measured at the different tests, are reported in the Table S3 of the Supporting Information.

The two previous experimental points were carried out at an anolyte flow rate per geometric anode surface area of 0.57 mL·min^{-1}·cm^{-2} in order to compare the results in terms of HCOO$^-$ production at the cathode with previous studies using a commercial Dimensionally Stable Anode (DSA/O_2) [DSA/O_2 (Ir-MMO (mixed metal oxide) on platinum), ElectroCell] catalysing the OER (Section 3.4). Nevertheless, these operation conditions did not allow detecting DHA as a high-value added product. This product suffers a degradation in alkaline medium [53] and, for this reason, it is required to reduce the DHA residence time in this media previous to the neutralisation with the acid solution (1.0 M H_2SO_4). Hence, various tests were carried out at different higher flow rate per unit of anode geometric area: 1.14, 1.17, 2.28 and 4.56 mL·min^{-1}·cm^{-2}, whose detailed results are reported in Tables S3-S11 as Supporting Information. The detailed results of this section, as well as the potentials measured at the different tests, are reported in the Table S3 of the Supporting Information.

Firstly, working with a constant catholyte flow rate per geometric cathode surface area and a current density of 0.57 mL·min^{-1}·cm^{-2} and 45 mA·cm^{-2}, respectively, when the anolyte flow per geometric surface area increases, the concentrations of the detected oxidation products generally decrease (Fig. S2 of the Supporting Information). In this sense, Fig. 7 depicts the results achieved in terms of Faradaic Efficiencies of each product (Fig. 7a) and production rates (Fig. 7b), showing the influence of the anolyte flow on the distribution of products from GOR obtained in the anode working in continuous mode at current densities of 45 mA·cm^{-2}. The analysis of Fig. 7 reveals that the formation of C1 products (especially of HCOO$^-$) is greatly favoured by increasing the anolyte flow. In contrast, both Faradaic Efficiencies and production rates of GLYC and LAC decrease when the anolyte flow rate is increased. For these anolyte flow rates, there are longer residence times of GOR intermediates such as GLAD or GLCA, which are in turn oxidised to compounds such as GLYC, or via other routes and through the subsequent Cannizaro rearrangement to LAC formation (Fig. 6). Moreover, the Cannizzaro reaction explains the absence of DHA in alkaline media under these operating conditions [53–55]. Besides, it is interesting to highlight that C3 oxidation products such as GLAD and MOX present a maximum in the production rates and Faradaic Efficiencies at anolyte flow rate per geometric surface area of 1.71 mL·min^{-1}·cm^{-2}, while, DHA as one of the intermediates of the GOR was not even detected at anolyte flow rates per geometric anode area of 0.57 mL·min^{-1}·cm^{-2}. However, by increasing this variable from 0.57 to 2.28 mL·min^{-1}·cm^{-2}, an important concentration of DHA of up to 51.50 mg·L^{-1} was detected, showing promising production rates and Faradaic Efficiencies of 217.29 µmol·m^{-2}·s^{-1} and 6.9%, respectively (Table S4 of Supporting Information).

A similar analysis of the influence of the anolyte flow rate per geometric anode surface area was carried out at catholyte flow rates per geometric anode surface area and current densities of 0.15 mL·min^{-1}·cm^{-2} and 90 mA·cm^{-2}, respectively. Fig. 7 illustrates the results achieved in terms of Faradaic Efficiencies (Fig. 7c) and production rates (Fig. 7d).

The general trends of the influence of anolyte flow were not very different to those detected in the previous analyses at 45 mA·cm^{-2}

(Fig. 7a and b). Regarding the C1 products, the maximum production of $HCOO^-$ was achieved with an anolyte flow rates per geometric anode surface area of 1.71 mL·min^{-1}·cm^{-2}, reaching values of Faradaic Efficiencies of 41.5% (Fig. 7a) and rates of 1458.00 μmol·m^{-2}·s^{-1} (Fig. 7d). On the other side, the highest values of Faradaic Efficiencies and production rates of CARB were obtained at higher anolyte flow rates per geometric anode surface area of 4.56 mL·min^{-1}·cm^{-2}. It has also been observed in Fig. 7 that increasing the anolyte flow rates per geometric anode surface area, the Faradaic Efficiencies and production rates of LAC and GLYC were reduced, as also happened in the previous experimental conditions. In a similar way, the Faradaic Efficiency and production rates of C3 products like MOX decrease at higher anolyte flow rates, reaching the best results of 6.2% and 59.30 μmol·m^{-2}·s^{-1}, respectively, at 0.57 mL·min^{-1}·cm^{-2}. This may be due to the fact that MOX is an oxidation by-product of hydroxypyruvate anion which in turn comes from the oxidation of DHA (Fig. 6). The two intermediates of the GOR such as GLAD and DHA present promising results in terms of Faradaic Efficiencies and production rate at anolyte flow rates per geometric anode surface area of 1.14 and 1.71 mL·min^{-1}·cm^{-2}, respectively (Fig. 7c). In this way, it seems that the two main reaction intermediates are in equilibrium, and that, in the presence of hydroxyl radicals, this equilibrium tends towards the formation of GLAD. For this reason, the DHA residence time in the alkaline media seems to be critical for further measurement.

3.3. Influence of the current density in the glycerol oxidation products distribution

After studying the influence of the anolyte flow rate per geometric anode surface area, this section is focused on the study of the influence of the current density on the distribution of glycerol oxidation products detected in the output stream of the anode compartment. According to the results of the analysis of the influence of the anolyte flow rate in the previous section, for the study of the influence of j, two intermediate flow rates of the considered range, in which the formation of the products of C3 oxidation was favoured, were taken as reference (i.e. 1.14 and 1.71 mL·min^{-1}·cm^{-2}). All previous tests were carried out at current densities of 45 and 90 mA·cm^{-2}, nevertheless, for a better understanding of the influence of this variable, further experiments were done at higher commercially-relevant current densities up to 200 mA·cm^{-2} [57].

Fig. 8 allows showing the influence of the current density in the glycerol oxidation products distribution obtained continuously working at anolyte flow rates per geometric anode surface area of 1.14 mL·min^{-1}·cm^{-2}. Longer glycerol oxidation products residence times implies a higher re-oxidation of the 3-carbon compounds of the GOR to simpler and lower value-added products such as CARB. For this reason, it is interesting to carry out the analysis of the influence of the current density at higher anolyte flow rates values, specifically from 1.14 mL·min^{-1}·cm^{-2}. Firstly, and as expected, the concentrations of the quantified oxidation products generally increase as the current density increases, with the exception of the C3 products DHA, GLAD and MOX (Fig. S4 as Supporting Information). This could be attributed to the fact that C3 products are re-oxidised faster towards simpler oxidation species at higher current densities, giving mainly C1 and C2 compounds.

Although C1 oxidation products such as $HCOO^-$ and CARB show an increase in their concentrations and rates with the current density, the Faradaic Efficiency for $HCOO^-$ decreases from 41.8% to 22.0% (Fig. 8a); in contrast, there is an upward trend in Faradaic Efficiency for CARB, whose FE increases dramatically from 45 to 90 mA·cm^{-2}, and then it stabilizes around 30% with further increase to 200 mA·cm^{-2}. Fig. 8a and b also show that the Faradaic Efficiencies and production rates of GLYC and LAC slightly increase working at higher current densities. GLYC is a product from the GLCA anion degradation which comes from the oxidation of GLAD intermediate (Fig. 6). On the other side, base-catalysed dehydration from GLAD intermediate to 2-hydroxypropenal, which tautomerizes to form pyruvaldehyde, may explain the LAC production through the subsequent Cannizzaro rearrangement [56,58]. Finally, Fig. 8 also reveals the decreasing trend of Faradaic Efficiencies of C3 oxidation products such as DHA, GLAD and MOX. The same was observed in the production rate of MOX, reaching the best yields at current densities of 45 mA·cm^{-2}. In contrast, the production rates of the main intermediates of the GOR (DHA and GLAD) obtain a peak at current densities of 90 mA·cm^{-2}. This observation supports that high current densities supplied to the cell lead to the oxidation of 3-carbon products to simpler 2-carbon and even 1-carbon products.

A similar analysis of the influence of the current density was carried out for a fixed anolyte flow rate per geometric anode surface area of 1.71 mL·min^{-1}·cm^{-2}. The results obtained, which are graphically summarised in Fig. 8c and d, confirm trends with the current density that are very similar to those observed for Qa/A of 1.14 mL·min^{-1}·cm^{-2}. As can be seen immediately again in the Fig. S5 of the Supporting information, the concentrations of the oxidation products in the anolyte output stream increase, with the exception of 3 carbons compounds such as MOX, GLAD and DHA, at higher current densities for a fixed value of the anolyte flow rate per geometric anode surface area of 1.71 mL·min^{-1}·cm^{-2}. It can also be highlighted that the highest glycerol conversions of 34.6% were obtained under these operating conditions and current densities of 200 mA·cm^{-2}, and as a consequence, the carbon balance also increased to 34.1% (Table S11 and Fig. S7 of the Supporting Information). In this sense, these results are in agreement with Liu and co-workers, who postulated that higher applied potentials could lead a more complete oxidation reaction [59]. Furthermore, observing the Fig. 8a and c, the remaining Faradaic Efficiency at relevant j of 200 mA·cm^{-2} (higher voltages) could be attributed to the more dominant OER side reaction and/or higher CO_2 production [60]. Both processes are influenced by the high electrode potential at the anode, particularly at high current density (200 mA·cm^{-2}). For lower current densities (45 and 90 mA·cm^{-2}), the effective potential is less positive and the FE of GOR tends to be close to 100%.

It is noteworthy that the Faradaic Efficiency towards $HCOO^-$ has a drop from 38.5% to 23.0% when the current density was increased from 45 to 200 mA·cm^{-2} (Fig. 8c). On the other side, an upward trend in the Faradaic Efficiency of CARB can also be observed, reaching the best percentages of 41.8% at current densities of 200 mA·cm^{-2}. Moreover, Fig. 8 clearly reveals that C1 oxidation products improve their yields in terms of the production rates by increasing the current density. CARB is the most oxidised product from GOR and it mainly comes from the oxidation of other C1 compound like $HCOO^-$ (Fig. 6) [61]. The analyses of Fig. 8 also show that the production rates and the Faradaic Efficiencies of GLYC and LAC grow as the current density increases. As already explained before, these two products are formed via different routes of the GLAD intermediate oxidation. The higher value-added oxidation products of 3 carbons such as GLAD and MOX present a downward trend in their Faradaic Efficiencies and production rates for higher current densities (Fig. 8c). The only exception is the DHA, where peaks in the production rate (196.76 μmol·m^{-2}·s^{-1}) and the Faradaic Efficiency (4.1%), were observed at current densities of 90 mA·cm^{-2}. This may be tentatively because the shorter residence time of DHA (as the anolyte flow rate per geometric anode surface area increased) in the alkaline medium affects the equilibrium GLAD formation prior to neutralisation. In addition, the higher presence of DHA in the anolyte outlet stream also explains the lower presence of MOX, which is a more oxidised compound from the subsequent degradation reactions of DHA in the alkaline medium (Fig. 6).

3.4. Glycerol oxidation vs OER: effect on the continuous $ERCO_2$ to formate

Finally, it is interesting to analyse the effect of using glycerol oxidation as the anode reaction instead of OER on the performance of the continuous $ERCO_2$ process to formate. For this, the results obtained in this work, coupling the GOR, will be compared with those obtained in

Table 1
Comparison of the performance of the continuous $ERCO_2$ to $HCOO^-$ using Pt/C-PE anode for GOR (this work) and using DSA/O_2 anode for OER [44] with the same experimental conditions in the filter-press reactor. A fixed value of anolyte flow rate per geometric anode surface area [Qa/A] of 0.57 $mL{\cdot}min^{-1}{\cdot}cm^{-2}$ was used in these tests.

Anode	Catholyte flow rate per geometric cathode surface area, Qc/A ($mL{\cdot}min^{-1}{\cdot}cm^{-2}$)	Current density, j ($mA{\cdot}cm^{-2}$)	Cell potential (V)	Anode potential (V)	Cathode potential (V)	[$HCOO^-$] ($g{\cdot}L^{-1}$)	FE for $HCOO^-$ (%)	Production rate of $HCOO^-$, r ($mmol{\cdot}m^{-2}{\cdot}s^{-1}$)	Energy consumption per kmol of $HCOO^-$, EC ($kWh{\cdot}kmol^{-1}$)	Standard deviation (%)
Pt/1C-PE	0.57	45	3.46	2.47	0.99	0.88	79	1.86	233	1.31
DSA/O_2			3.00	1.96	1.04	0.90	81	1.90	197	3.98
Pt/C-PE	0.15	90	4.51	3.26	1.25	7.17	85	4.00	283	7.10
DSA/O_2			3.10	1.80	1.30	7.51	89	4.18	186	6.49

our previous investigations, under the same operating conditions, but with a DSA/O_2 as anode [44]. The results used to make the comparison are detailed in Table 1.

First, working with a catholyte flow per geometric surface area of 0.57 $mL{\cdot}min^{-1}{\cdot}cm^{-2}$ and a current density of 45 $mA{\cdot}cm^{-2}$, similar $HCOO^-$ concentrations and Faradaic Efficiencies for $HCOO^-$ were obtained in the cathode of approximately 0.90 $g{\cdot}L^{-1}$ and 80%, respectively, in comparison with previous studies carried out with a DSA/O_2, as shown in Table 1. Nevertheless, the energy consumption per kmol of $HCOO^-$ noticeably increased by more than 26%, which can be attributed to the higher anode potentials that those reported previously with DSA/O_2.

To confirm the results, additional tests were performed at a higher current density of 90 $mA{\cdot}cm^{-2}$ and a catholyte flow per geometric surface area of 0.15 $mL{\cdot}min^{-1}{\cdot}cm^{-2}$. In this sense, product concentrations, production rates and Faradaic Efficiencies for $HCOO^-$ up to 7.17 $g{\cdot}L^{-1}$, 4.00 $mmol{\cdot}m^{-2}{\cdot}s^{-1}$, and 85%, respectively, were observed in the cathode, which are close to those obtained by using the DSA/O_2 at these operating conditions. The energy consumptions per kmol of $HCOO^-$ were even higher (above 50%) than those obtained with the OER using the DSA/O_2 due to the rise of anode potential. Finally, in the tests carried out under commercially relevant current density up to 200 $mA{\cdot}cm^{-2}$, the $HCOO^-$ productions of the cathode attained were similar to those achieved by DSA/O_2 of previous works [44], obtaining $HCOO^-$ concentrations of approximately 18 $g{\cdot}L^{-1}$, as can be checked in the Table S3 of the Supporting Information.

The figures of merit achieved in the cathodic compartment of the electrochemical reactor are promising, and they demonstrated that the coupling of the GOR with the $ERCO_2$ allows achieving similar results in comparison with previous studies in the group with a DSA/O_2 to carry out the OER in the anode.

4. Conclusions

This study reports a novel coupling of GOR to high value-added products to the $ERCO_2$ reaction to $HCOO^-$ both reactions working in continuous mode. The experimental setup, which was carefully designed for this purpose, represents an innovative approach for the continuous co-production of $HCOO^-$ and higher value-added carbon products. Interestingly, under the same experimental conditions of previous works, several glycerol oxidation products with 1 carbon (CARB, $HCOO^-$), 2 carbons (GLYC) and 3 carbons (LAC, GLAD, MOX) have been detected and quantified, achieving glycerol conversions and carbon balances of 2.45% and 1.15%, respectively. In addition, a study of the influence of the anolyte flow rate per geometric anode surface area has been carried out, identifying another interesting C3 oxidation product such as DHA, which undergoes degradation reactions in the alkaline medium used. This study has also made possible to establish different trends in the distribution of glycerol oxidation products, showing that C3 products of high added value are obtained at higher anolyte flow rates per geometric anode surface area. A clear example of this is DHA, which has been measured in concentrations of up to 51 $mg{\cdot}L^{-1}$ at anolyte flow rates per geometric anode surface area of 2.28 $mL{\cdot}min^{-1}{\cdot}cm^{-2}$. On the other hand, an analysis of the influence of current density on the distribution of oxidation products has also been carried out. In this respect, relatively high current densities are required for relevant $HCOO^-$ productions at the cathode. Under these high current densities of up to 200 $mA{\cdot}cm^{-2}$ simpler oxidation products such as $HCOO^-$ or CARB are produced in higher amounts at the expense of the formation of intermediate products such as DHA or GLAD. Finally, it is important to remark that the figures of merit of the $HCOO^-$ production (cathodic reaction) remain at similar values to those obtained with the same experimental system with a DSA/O_2 anode catalysing the OER under the same operating conditions of previous studies. In this context, Faradaic Efficiencies towards $HCOO^-$ of up to 85% can be obtained at the cathode at current densities of 90 $mA{\cdot}cm^{-2}$ while GOR is taking place at the anode.

This study represents a step forward in this field since up to now there are not available approaches in the continuous electrochemical production of $HCOO^-$ from CO_2 coupling the single pass glycerol oxidation to high value-added products of 3 carbons. Further research is still required in order to improve the anodic reaction selectivity to higher value-added products without compromising the cathode performance, especially operating at high current densities.

CRediT authorship contribution statement

Kevin Fernández-Caso: Conceptualization, Methodology, Validation, Investigation, Writing – original draft, Conceptualization, Data curation. **Ailen Peña-Rodríguez:** Methodology, Validation, Investigation, Writing – review & editing. **Jose Solla-Gullón:** Writing – review & editing, Supervision, Project administration, Funding acquisition, **Vicente Montiel:** Writing – review & editing, Supervision, Project administration, Funding acquisition. **Guillermo Díaz-Sainz**: Conceptualization, Methodology, Investigation, Data curation, Writing – original draft, Writing – review & editing, Supervision. **Manuel Alvarez-Guerra:** Conceptualization, Methodology, Writing – original draft, Writing – review & editing, Supervision, Project administration, Funding acquisition. **Angel Irabien:** Writing – review & editing, Supervision, Project administration, Funding acquisition.

Declaration of Competing Interest

The authors declare that they have no known competing financial interests or personal relationships that could have appeared to influence the work reported in this paper.

Data Availability

No data was used for the research described in the article.

Acknowledgements

The authors gratefully acknowledge financial support through projects PID2019–108136RB-C31, PID2019–108136RB-C32 and PID2020–112845RB-I00 (AEI/10.13039/501100011033).

Appendix A. Supporting information

Supplementary data associated with this article can be found in the online version at doi:10.1016/j.jcou.2023.102431.

References

[1] W. Da Silva Freitas, A. D'Epifanio, B. Mecheri, Electrocatalytic CO_2 reduction on nanostructured metal-based materials: challenges and constraints for a sustainable pathway to decarbonization, J. CO_2 Util. 50 (2021), 101579.
[2] S. Garg, M. Li, A.Z. Weber, L. Ge, L. Li, V. Rudolph, G. Wang, T.E. Rufford, Advances and challenges in electrochemical CO_2 reduction processes: an engineering and design perspective looking beyond new catalyst materials, J. Mater. Chem. A 8 (2020) 1511–1544.
[3] X. Yu, A. Manthiram, Catalyst-selective, scalable membraneless alkaline direct formate fuel cells, Appl. Catal. B Environ. 165 (2015) 63–67.
[4] M. Ren, Y. Kang, W. He, Z. Zou, X. Xue, D.L. Akins, H. Yang, S. Feng, Origin of performance degradation of palladium-based direct formic acid fuel cells, Appl. Catal. B Environ. 104 (2011) 49–53.
[5] D. Du, R. Lan, J. Humphreys, S. Tao, Progress in inorganic cathode catalysts for electrochemical conversion of carbon dioxide into formate or formic acid, J. Appl. Electrochem 47 (2017) 661–678.
[6] B. Ávila-Bolívar, R. Cepitis, M. Alam, J.M. Assafrei, K. Ping, J. Aruväli, A. Kikas, V. Kisand, S. Vlassov, M. Käärik, J. Leis, V. Ivaništšev, P. Starkov, V. Montiel, J. Solla-Gullón, N. Kongi, CO_2 reduction to formate on an affordable bismuth metal-organic framework based catalyst, J. CO_2 Util. 59 (2022), 101937.
[7] B. Ávila-Bolívar, V. Montiel, J. Solla-Gullón, On the activity and stability of Sb_2O_3/Sb nanoparticles for the electroreduction of CO_2 toward formate, J. Electroanal. Chem. 895 (2021), 115440.
[8] A. Löwe, C. Rieg, T. Hierlemann, N. Salas, D. Kopljar, N. Wagner, E. Klemm, Influence of temperature on the performance of gas diffusion electrodes in the co2 reductionReaction, ChemElectroChem 6 (2019) 4497–4506.
[9] A. Löwe, M. Schmidt, F. Bienen, D. Kopljar, N. Wagner, E. Klemm, Optimizing reaction conditions and gas diffusion electrodes applied in the CO_2 reduction reaction to formate to reach current densities up to 1.8 A cm^{-2}, ASC Sustain. Chem. Eng. 9 (2021) 4213–4223.
[10] J. Albo, M. Alvarez-guerra, A. Irabien, Electro-, Photo-, and Photoelectro-chemical Reduction of CO_2, in: Wey Yang Teoh, A. Urakawa, Y.H. Ng, P. Sit (Eds.), Heterog. Catal. Adv. Des. Charact. Appl. II, Wiley-VCH, 2021, pp. 649–669.
[11] L. Li, A. Ozden, S. Guo, F. Pelayo García de Arquer, C. Wang, M. Zhang, J. Zhang, H. Jiang, W. Wang, H. Dong, D. Sinton, E.H. Sargent, M. Zhong, Stable, active CO_2 reduction to formate via redox-modulated stabilization of active sites, Nat. Commun. 12 (2021) 5223.
[12] C. Xia, P. Zhu, Q. Jiang, Y. Pan, W. Liang, E. Stavitsk, H.N. Alshareef, H. Wang, Continuous production of pure liquid fuel solutions via electrocatalytic CO_2 reduction using solid-electrolyte devices, Nat. Energy 4 (2019) 776–785.
[13] L. Fan, C. Xia, P. Zhu, Y. Lu, H. Wang, Electrochemical CO_2 reduction to high-concentration pure formic acid solutions in an all-solid-state reactor, Nat. Commun. 11 (2020) 3633.
[14] G. Díaz-Sainz, M. Alvarez-Guerra, B. Ávila-Bolívar, J. Solla-Gullón, V. Montiel, A. Irabien, Improving trade-offs in the figures of merit of gas-phase single-pass continuous CO_2 electrocatalytic reduction to formate, Chem. Eng. J. 405 (2021), 126965.
[15] H. Yang, J.J. Kaczur, S.D. Sajjad, R.I. Masel, Electrochemical conversion of CO_2 to formic acid utilizing SustainionTM membranes, J. CO_2 Util. 20 (2017) 208–217.
[16] H. Yang, J.J. Kaczur, S.D. Sajjad, R.I. Masel, Performance and long-term stability of CO_2 conversion to formic acid using a three-compartment electrolyzer design, J. CO_2 Util. 42 (2020), 101349.
[17] R.I. Masel, Z. Liu, H. Yang, J.J. Kaczur, D. Carrillo, S. Ren, D. Salvatore, C. P. Berlinguette, An industrial perspective on catalysts for low-temperature CO_2 electrolysis, Nat. Nanotechnol. 16 (2021) 118–128.
[18] M. Rumayor, A. Dominguez-Ramos, A. Irabien, Environmental and economic assessment of the formic acid electrochemical manufacture using carbon dioxide: Influence of the electrode lifetime, Sustain. Prod. Consum. 18 (2019) 72–82.
[19] M. Rumayor, A. Dominguez-Ramos, P. Perez, A. Irabien, A techno-economic evaluation approach to the electrochemical reduction of CO_2 for formic acid manufacture, J. CO_2 Util. 34 (2019) 490–499.
[20] A. Irabien, Manuel Alvarez-Guerra, J. Albo, A. Dominguez-Ramos, Electrochemical conversion of CO_2 to value-added products, in: C.A. Martínez-Huitle, M.A. Rodrigo, O. Scialdone (Eds.), Electrochem. Water Wastewater Treat, Elsevier, 2018, pp. 29–59.
[21] X. Wang, F. Li, W.-J. Yin, Y. Si, M. Miao, X. Wang, Y. Fu, Atomically dispersed Sn modified with trace sulfur species derived from organosulfide complex for electroreduction of CO_2, Appl. Catal. B Environ. 304 (2022), 120936.
[22] M. Fan, S. Prabhudev, S. Garbarino, J. Qiao, G.A. Botton, D.A. Harrington, A. C. Tavares, D. Guay, Uncovering the nature of electroactive sites in nano architectured dendritic Bi for highly efficient CO_2 electroreduction to formate, Appl. Catal. B Environ. 274 (2020), 119031.
[23] I. Merino-Garcia, L. Tinat, J. Albo, M. Alvarez-Guerra, A. Irabien, O. Durupthy, V. Vivier, C.M. Sánchez-Sánchez, Continuous electroconversion of CO_2 into formate using 2 nm tin oxide nanoparticles, Appl. Catal. B Environ. 297 (2021), 120447.
[24] G. Díaz-Sainz, K. Fernández-Caso, T. Lagarteira, S. Delgado, M. Alvarez-Guerra, A. Mendes, A. Irabien, Coupling continuous CO_2 electroreduction to formate with efficient Ni-based anodes, J. Environ. Chem. Eng. 11 (2023), 109171.
[25] J. Na, B. Seo, J. Kim, C. Woo Lee, H. Lee, Y. Jeong Hwang, B. Koun Min, D. Ki Lee, H.-S. Oh, U. Lee, General technoeconomic analysis for electrochemical coproduction coupling carbon dioxide reduction with organic oxidation, Nat. Commun. 10 (2019) 5193.
[26] S. Verma, S. Lu, P.J.A. Kenis, Co-electrolysis of CO_2 and glycerol as a pathway to carbon chemicals with improved technoeconomics due to low electricity consumption, Nat. Energy 4 (2019) 466–474.
[27] M. Rumayor, A. Domínguez-Ramos, Á. Irabien, Feasibility analysis of a CO_2 recycling plant for the decarbonization of formate and dihydroxyacetone production, Green. Chem. 23 (2021) 4840–4851.
[28] S. Sabatino, A. Galia, G. Saracco, O. Scialdone, Development of an electrochemical process for the simultaneous treatment of wastewater and the conversion of carbon dioxide to higher value products, ChemElectroChem 4 (2017) 150–159.
[29] Q. Wang, X. Wang, C. Wu, Y. Cheng, Q. Sun, H. Yu, Enhanced electroreduction of CO_2 and simultaneous degradation of organic pollutants using a Sn-based carbon nanotubes/carbon black hybrid gas diffusion cathode, J. CO_2 Util. 26 (2018) 425–433.
[30] M. Bevilacqua, J. Filippi, A. Lavacchi, A. Marchionni, H.A. Miller, W. Oberhauser, E. Vesselli, F. Vizza, Energy savings in the conversion of CO_2 to fuels using an electrolytic device, Energy Technol. 2 (2014) 522–525.
[31] D. Wu, J. Hao, Z. Song, X.Z. Fu, J.L. Luo, All roads lead to Rome: an energy-saving integrated electrocatalytic CO_2 reduction system for concurrent value-added formate production, Chem. Eng. J. 412 (2021), 127893.
[32] Y. Zhang, J. Lan, F. Xie, M. Peng, J. Liu, T.-S. Chan, Y. Tan, Aligned InS nanorods for efficient electrocatalytic carbon dioxide reduction, ACS Appl. Mater. Interfaces 14 (2022) 25257–25266.
[33] M. Li, T. Wang, W. Zhao, S. Wang, Y. Zou, A pair-electrosynthesis for formate at ultra-low voltage via coupling of CO_2 reduction and formaldehyde oxidation, Nano-Micro Lett. 14 (2022) 1–17.
[34] G. Dodekatos, S. Schu¨, H. Tu¨ Ysu¨, Recent advances in Thermo-, Photo-, and electrocatalytic glycerol oxidation, ACS Catal (2018) 6301–6333.
[35] A.C. Garcia, Y.Y. Birdja, G. Tremiliosi-Filho, M.T.M. Koper, Glycerol electro-oxidation on bismuth-modified platinum single crystals, J. Catal. 346 (2017) 117–124.
[36] W. Hu, D. Knight, B. Lowry, A. Varma, Selective oxidation of glycerol to dihydroxyacetone over Pt-Bi/C catalyst: Optimization of catalyst and reaction conditions, Ind. Eng. Chem. Res. 49 (2010) 10876–10882.
[37] S. Bagheri, N.M. Julkapli, W.A. Yehye, Catalytic conversion of biodiesel derived raw glycerol to value added products, Renew. Sustain. Energy Rev. 41 (2015) 113–127.
[38] X. Han, H. Sheng, C. Yu, T.W. Walker, G.W. Huber, J. Qiu, S. Jin, Electrocatalytic oxidation of glycerol to formic acid by $CuCo_2O_4$ spinel oxide nanostructure catalysts, ACS Catal. 10 (2020) 6741–6752.
[39] G. Wang, J. Chen, K. Li, J. Huang, Y. Huang, Y. Liu, X. Hu, B. Zhao, L. Yi, T. W. Jones, Z. Wen, Cost-effective and durable electrocatalysts for Co-electrolysis of CO_2 conversion and glycerol upgrading, Nano Energy 92 (2022), 106751.
[40] M.S.E. Houache, R. Safari, U.O. Nwabara, T. Rafaïdeen, G.A. Botton, P.J.A. Kenis, S. Baranton, C. Coutanceau, E.A. Baranova, Selective electrooxidation of glycerol to formic acid over carbon supported $Ni_{1-x}M_x$(M = Bi, Pd, and Au) nanocatalysts and coelectrolysis of CO_2, ACS Appl. Energy Mater. 3 (2020) 8725–8738.
[41] M.A. Khan, S.K. Nabil, T. Al-Attas, N.G. Yasri, S. Roy, M.M. Rahman, S. Larter, P. M. Ajayan, J. Hu, M.G. Kibria, Zero-crossover electrochemical CO_2 reduction to ethylene with co-production of valuable chemicals, Chem. Catal. 2 (2022) 2077–2095.
[42] Y. Pei, Z. Pi, H. Zhong, J. Cheng, F. Jin, Glycerol oxidation-assisted electrochemical CO_2 reduction for the dual production of formate, J. Mater. Chem. A 10 (2022) 1309–1319.
[43] X. Guo, S.-M. Xu, H. Zhou, Y. Ren, R. Ge, M. Xu, L. Zheng, X. Kong, M. Shao, Z. Li, H. Duan, Engineering Hydrogen Generation Sites to Promote Electrocatalytic CO_2 Reduction to Formate, ACS Catal. 12 (2022) 10551–10559.
[44] G. Díaz-Sainz, M. Alvarez-Guerra, J. Solla-Gullón, L. García-Cruz, V. Montiel, A. Irabien, CO_2 electroreduction to formate: continuous single-pass operation in a filter-press reactor at high current densities using Bi gas diffusion electrodes, J. CO_2 Util. 34 (2019) 12–19.
[45] A. Del Castillo, M. Alvarez-Guerra, J. Solla-Gullón, A. Sáez, V. Montiel, A. Irabien, Electrocatalytic reduction of CO_2 to formate using particulate Sn electrodes: Effect of metal loading and particle size, Appl. Energy 157 (2015) 165–173.
[46] G. Díaz-Sainz, M. Alvarez-Guerra, J. Solla-Gullón, L. García-Cruz, V. Montiel, A. Irabien, Catalyst coated membrane electrodes for the gas phase CO_2 electroreduction to formate, Catal. Today 346 (2020) 58–64.
[47] G. Díaz-Sainz, M. Alvarez-Guerra, A. Irabien, Continuous electroreduction of CO_2 towards formate in gas-phase operation at high current densities with an anion exchange membrane, J. CO_2 Util. (2021), 101822.
[48] B. Ávila-Bolívar, L. García-Cruz, V. Montiel, J. Solla-Gullón, Electrochemical reduction of CO_2 to formate on easily prepared carbon-supported Bi nanoparticles, Molecules 24 (2019) 2032.

[49] J. Solla-Gullón, P. Rodríguez, E. Herrero, A. Aldaz, J.M. Feliu, Surface characterization of platinum electrodes, Phys. Chem. Chem. Phys. 10 (2008) 1359–1373.
[50] F.J. Vidal-Iglesias, R.M. Arán-Ais, J. Solla-Gullón, E. Herrero, J.M. Feliu, Electrochemical characterization of shape-controlled Pt nanoparticles in different supporting electrolytes, ACS Catal. 2 (2012) 901–910.
[51] A. Sáez, J. Solla-Gullón, E. Expósito, V. Montiel, A. Aldaz, Gold supported catalytic layer: An intermediate step between fundamental and applied fuel cell studies, Electrochim. Acta 54 (2009) 7071–7077.
[52] X. Huang, Y. Zou, J. Jiang, Electrochemical oxidation of glycerol to dihydroxyacetone in borate buffer: enhancing activity and selectivity by borate−polyol coordination chemistry, ACS Sustain. Chem. Eng. 9 (2021) 14470–14479.
[53] Y.Y. Birdja, M.T.M. Koper, The importance of cannizzaro-type reactions during electrocatalytic reduction of carbon dioxide, J. Am. Chem. Soc. 139 (2017) 2030–2034.
[54] C.C. Lima, M.V.F. Rodrigues, A.F.M. Neto, C.R. Zanata, C.T.G.V.M.T. Pires, L. S. Costa, J. Solla-Gullón, P.S. Fernández, Highly active Ag/C nanoparticles containing ultra-low quantities of sub-surface Pt for the electrooxidation of glycerol in alkaline media, Appl. Catal. B Environ. 279 (2020), 119369.
[55] T. Li, D.A. Harrington, An overview of glycerol electrooxidation mechanisms on Pt, Pd and Au, ChemSusChem 14 (2021) 1472–1495.
[56] M.S.E. Houache, K. Hughes, R. Safari, G.A. Botton, E.A. Baranova, Modification of nickel surfaces by bismuth: effect on electrochemical activity and selectivity toward glycerol, ACS Appl. Mater. Interfaces 12 (2020) 15095–15107.
[57] T. Burdyny, W.A. Smith, CO_2 reduction on gas-diffusion electrodes and why catalytic performance must be assessed at commercially-relevant conditions, Energy Environ. Sci. 12 (2019) 1442–1453.
[58] M. Batista Cordeiro Souza, Development of p-block adatom-modified platinum electrocatalysts for the electrochemical conversion of glycerol in alkaline medium (PhD thesis), University of Campinas,, Sao Paulo, 2022.
[59] C. Liu, M. Hirohara, T. Maekawa, R. Chang, T. Hayashi, C.Y. Chiang, Selective electro-oxidation of glycerol to dihydroxyacetone by a non-precious electrocatalyst – CuO, Appl. Catal. B Environ. 265 (2020), 118543.
[60] H. Wan, C. Dai, L. Jin, S. Luo, F. Meng, G. Chen, Y. Duan, C. Liu, Q. Xu, J. Lu, Z. J. Xu, Electro-Oxidation of glycerol to high-value-added C1-C3 products by iron-substituted spinel zinc cobalt oxides, ACS Appl. Mater. Interfaces 14 (2022) 14293–14301.
[61] Y. Zhou, Y. Shen, J. Xi, X. Luo, Selective electro-oxidation of glycerol to dihydroxyacetone by PtAg skeletons, Appl. Mater. Interfaces 11 (2019) 28953–28959.